RSC Advances

PAPER

View Article Online
View Journal | View Issue

Cite this: *RSC Adv.*, 2019, **9**, 11005

Synthesis and enhanced visible light photocatalytic CO_2 reduction of $BiPO_4$–$BiOBr_xI_{1-x}$ p–n heterojunctions with adjustable energy band

Hao Yong Yin,[a] Yi Fan Zheng[b] and Xu Chun Song *[c]

Received 25th February 2019
Accepted 3rd April 2019

DOI: 10.1039/c9ra01416k

rsc.li/rsc-advances

A series of novel $BiPO_4$–$BiOBr_xI_{1-x}$ p–n heterojunctions were successfully prepared by a facile solvothermal method. The morphology, structure and optical properties of photocatalysts were characterized by scanning electron microscopy (SEM), X-ray diffraction (XRD) and ultraviolet visible diffuse reflectance spectroscopy. The visible light photocatalytic activities of $BiPO_4$–$BiOBr_xI_{1-x}$ heterojunctions were investigated by photocatalytically reducing CO_2. After 4 hours of irradiation, the 5% $BiPO_4$–$BiOBr_{0.75}I_{0.25}$ heterojunction showed the highest photocatalytic activity with the yields of CO and CH_4 up to 24.9 and 9.4 μmol g_{cat}^{-1} respectively. The improved photocatalytic activity may be due to the formation of $BiPO_4$–$BiOBr_xI_{1-x}$ p–n heterojunctions which can effectively restrict the recombination rate of the photoexcited charge carriers. Moreover, the energy band structure of $BiPO_4$–$BiOBr_xI_{1-x}$ heterojunctions could be easily adjusted by changing the mole ratio of I and Br. The possible mechanism of the enhancement of the photocatalytic performance was also proposed based on experimental and theoretical analysis. The present study may provide a rational strategy to design highly efficient heterojunctions with an adjustable energy band for environmental treatment and energy conversion.

1. Introduction

Nowadays, the global energy shortage and alarming level of CO_2 in the atmosphere have brought more and more pressure for human beings. The photocatalytic reduction of CO_2 using semiconductor-based photocatalysts was considered as a promising approach to eliminate the greenhouse effect, which may also provide valuable fuels such as CO and CH_4. However, the widely used photocatalyst TiO_2[1–7] can only respond to ultraviolet light due to its larger energy band gap (3.2 V), which limits its effective utilization of solar light. Recently, bismuth-based photocatalysts, such as BiOX (X = Cl, Br, I),[8–12] $Bi_2O_2CO_3$,[13] BiOCOOH,[14] Bi_2WO_6,[15–17] Bi_2MoO_6,[18,19] $BiPO_4$,[20–24] and $BiVO_4$,[25] have been intensively investigated and were considered as very promising semiconductor photocatalysts due to their excellent photocatalytic efficiency in decomposing different kinds of organic pollutants.

Recently, $BiPO_4$, as a new n-type photocatalyst has been intensively studied due to its excellent photocatalytic performance, electronic properties, stable chemical structure, high specific surface area and low cost. The monoclinic $BiPO_4$ was reported to have higher photocatalytic activity than that of TiO_2 for organic pollutants degradation under UV light irradiation.[26] Moreover, the inductive effect of $PO_4{}^{3-}$ can benefit the separation of photo-induced electron–holes pairs, which is very important in photocatalytic process.[27,28] Despite possessing a higher photocatalytic activity, the further application of $BiPO_4$ was still limited by its wider band gap, which can only respond the ultraviolet light accounting for 4% of total solar irradiation.[29] Therefore, many methods have been investigated to improve the visible light response of $BiPO_4$ based photocatalysts. Among these methods, modification of $BiPO_4$ surface with suitable narrow band-gap was considered to be a promising strategy to realize its visible light response.

Bismuth oxyhalides compounds BiOX (X = Cl, Br, I), as a kind of p-type photocatalysis active materials, have recently attracted more attention due to their high photocatalytic activity, suitable band gap, high stability, electronic properties, optical properties and non-toxicity.[30] BiOX has the internal structure of $(Bi_2O_2)^{2+}$ layers interleaved by double slabs of X ions with weak van der Waals interactions along the *c*-axis, which can form the internal electric fields between $(Bi_2O_2)^{2+}$ layers and X slabs. The formed static electric fields can promote effective separation of photogenerated electron–hole pairs, which is a key factor for the improvement of the photocatalytic activity.[31,32] However, the photoelectrochemical properties of pure BiOX are still unsatisfactory for practical applications due

---

[a] *College of Materials & Environmental Engineering, Hangzhou Dianzi University, Hangzhou, 310018, P. R. China*

[b] *Research Center of Analysis and Measurement, Zhejiang University of Technology, Hangzhou 310014, P. R. China*

[c] *Department of Chemistry, Fujian Normal University, Fuzhou 350007, P. R. China. E-mail: songxuchunfj@163.com; Fax: +86-591-83465376; Tel: +86-591-87441126*

to the poor light absorption, utilization and stabilization. Therefore, many strategies have been employed to improve the photoelectrochemical properties of BiOX, such as the morphology controlling, semiconductor combining and noble metals doping. Especially, forming a series of solid solutions has been recently proved to be a promising method improving the photocatalytic activity of BiOX (X = Cl, Br, I). For instance, highly solar light induced photocatalytic activities were obtained on the high quality $BiOCl_xI_{1-x}$ *via* a hydrothermal process.[33] Moreover, the $BiOCl_xBr_{1-x}$[34–36] and $BiOBr_xI_{1-x}$[37] solid solutions with improved photocatalytic activities have also been successfully synthesized. As is known that constructing p–n heterojunction photocatalysts is another efficient method to improve the photocatalytic activity. The p–n heterojunctions can increase the separation probability of photogenerated electron–hole pairs by an additional internal electric field formed in the photocatalysts, which is beneficial for the photocatalytic reaction. Therefore, the construction of p–n heterojunctions between solid solutions of $BiOBr_xI_{1-x}$ and $BiPO_4$ may result in highly improved photocatalytic performance.

In this work, a series of novel and energy band adjustable $BiPO_4$–$BiOBr_xI_{1-x}$ ($x = 0, 0.25, 0.5, 0.75$ and 1) composites with p–n heterojunction structures were synthesized by a simple solvothermal method. The band gap structures of the $BiPO_4$–$BiOBr_xI_{1-x}$ p–n heterojunctions can be easily adjusted by changing the ratio of Br and I in the solid solution of $BiOBr_xI_{1-x}$, which may further adjust and optimize the photocatalytic performance of the catalyst. The photocatalytic activity of the $BiPO_4$–$BiOBr_xI_{1-x}$ p–n heterojunction, pure $BiPO_4$ and $BiOBr_xI_{1-x}$ solid solutions, was evaluated by reduction of CO_2 under visible light irradiation ($\lambda > 420$ nm). The 5% $BiPO_4$–$BiOBr_{0.75}I_{0.25}$ heterojunction showed the highest photocatalytic activity in the reduction of CO_2. Moreover, a possible visible light induced photocatalytic mechanism on the $BiPO_4$–$BiOBr_xI_{1-x}$ p–n heterojunction was also proposed according to the experimental results.

2. Experimental section

2.1 Synthesis of $BiPO_4$ precursor

All the reagents were of analytical grade and used without further purification. The $BiPO_4$ precursor was synthesized *via* a hydrothermal method. Typically, 5 mmol of $Bi(NO_3)_3 \cdot 5H_2O$ was firstly dissolved into 20 mL distilled water with strongly stirring. At the same time, 5 mmol of $NaH_2PO_4 \cdot 2H_2O$ was dissolved into 20.0 mL deionized water. After that, the $NaH_2PO_4 \cdot 2H_2O$ solution was added dropwise into the $Bi(NO_3)_3 \cdot 5H_2O$ solution under strongly stirring. After 30 min of stirring, the mixed suspension was transferred into a 50 mL of Teflon-lined stainless steel autoclave and maintained at 140 °C for 12 h. After cooling down to room temperature, the $BiPO_4$ solid products were collected *via* centrifugal separation, washed by deionized water for several times, and then dried at 60 °C in oven.

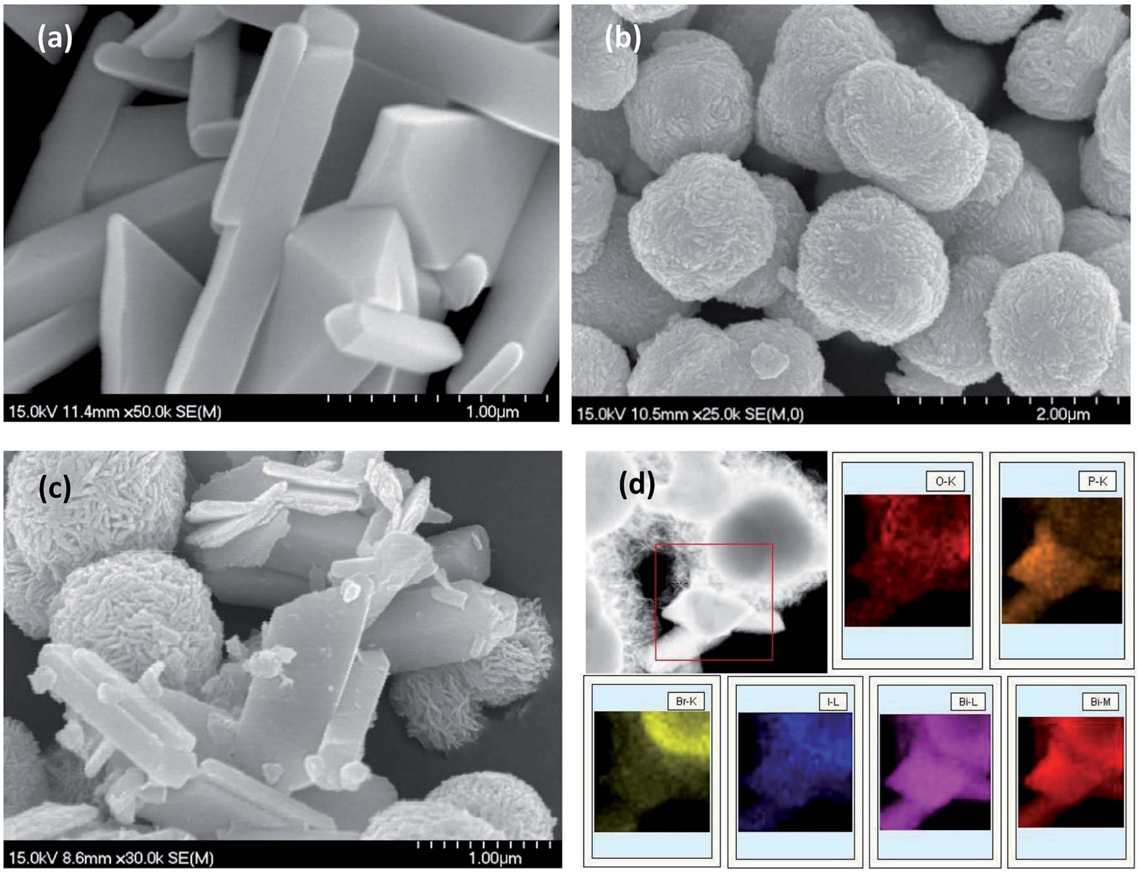

Fig. 1 SEM images of (a) $BiPO_4$, (b) $BiOBr_{0.75}I_{0.25}$, (c) 5% $BiPO_4$–$BiOBr_{0.75}I_{0.25}$, (d) the element mapping of 5% $BiPO_4$–$BiOBr_{0.75}I_{0.25}$.

2.2 Preparation of $BiPO_4$–$BiOBr_xI_{1-x}$heterojunctions

A series of $BiPO_4$–$BiOBr_xI_{1-x}$ heterojunctions, $BiOBr_xI_{1-x}$ ($x = 0$, 0.25, 0.5, 0.75 and 1) with different mole ratios of $BiPO_4$ (2%, 5% and 10%), were prepared *via* a facile solvothermal method. Taking 5% $BiPO_4$–$BiOBr_{0.75}I_{0.25}$ ($x = 0.75$) as an example, 5 mmol of $Bi(NO_3)_3\cdot 5H_2O$ was firstly dispersed into 20 mL ethylene glycol (EG) to form the solution A. Then 0.08 g $BiPO_4$ was added into the solution A under strongly stirring to form the solution B. Meanwhile, 3.75 mmol KBr and 1.25 mmol KI were dissolved into 20 mL EG to form the solution C. After 30 min of continuous stirring, the solution C was added dropwise into solution B with stirring for another 30 min. The resulting mixture was then transferred into a 50 mL a Teflon-lined stainless steel autoclave, and the temperature was maintained at 140 °C for 12 h. After cooling down to room temperature, the resulting product was separated by centrifugation and washed with deionized water for several times, then dried at 60 °C. Similarly, a series of $BiPO_4$–$BiOBr_xI_{1-x}$ ($x = 0$, 0.25, 0.5, 0.75 and 1) heterojunctions with different mole ratios of $BiPO_4$ (2%, 5% and 10%) were synthesized in the same process by adjusting the ratios of corresponding elements. For comparison, $BiOBr_xI_{1-x}$ was also prepared under the same procedure in the absence of $BiPO_4$.

2.3 Characterization

Crystal structure of the as-synthesized samples was recorded on a Thermo ARL SCINTAG X'TRA with Cu Kα X-ray source (λ = 0.154 056 nm) operating at 40 kV and 40 mA. The morphologies of $BiOBr_xI_{1-x}$ and $BiPO_4$–$BiOBr_xI_{1-x}$ heterojunctions were observed by a Hitachi S-4700 scanning electron microscopy (SEM). The UV-vis diffuse reflectance spectra (DRS) of the as-obtained samples were measured on a Lambda 850 UV-vis spectrophotometer. The X-ray photoelectrons spectroscopy (XPS, ThermoESCALAB250, USA) was employed to examine the electric potentials of the valence band (VB). The electrochemical workstation (CHI-660E, China) with a standard three-electrode chemical cell was used to measure the photocurrent of samples. ITO glass coupled with the as-synthesized samples (0.1 mg) served as the working electrode. The counter electrode and reference electrode were platinum wire and Ag/AgCl electrode, respectively. 0.1 M Na_2SO_4 aqueous solution was used as electrolyte.

2.4 Photocatalytic experiments

The photocatalytic activity of all the samples was estimated by photocatalytic CO_2 conversion under visible light irradiation. Typically, 0.05 g of the photocatalyst was firstly dispersed uniformly onto a glass sheet, and then transferred into the reaction cell. Prior to the light irradiation, the air in reaction cell was completely removed by vacuum-treatment. After that 1 atm mixture gas of CO_2/H_2O serving as reaction gas was introduced into the reaction cell. Then the reaction system was illuminated by a PLS-SXE300 Xe lamp (1900 mW cm^{-2}) with a 420 nm cut off filter. After 4 h visible light irradiation, 1 mL of gas was taken from the reaction cell. Finally, the amounts of CO and CH_4 in the reactor were analyzed by a GC (Agilent 7890) with a flame ionization detector (FID, Porapak N 80/100 columns).

3. Results and discussion

In order to investigate the morphology and microstructure of the as-obtained products, the $BiPO_4$, $BiOBr_{0.75}I_{0.25}$ and 5% $BiPO_4$–$BiOBr_{0.75}I_{0.25}$ composites were characterized by SEM, as

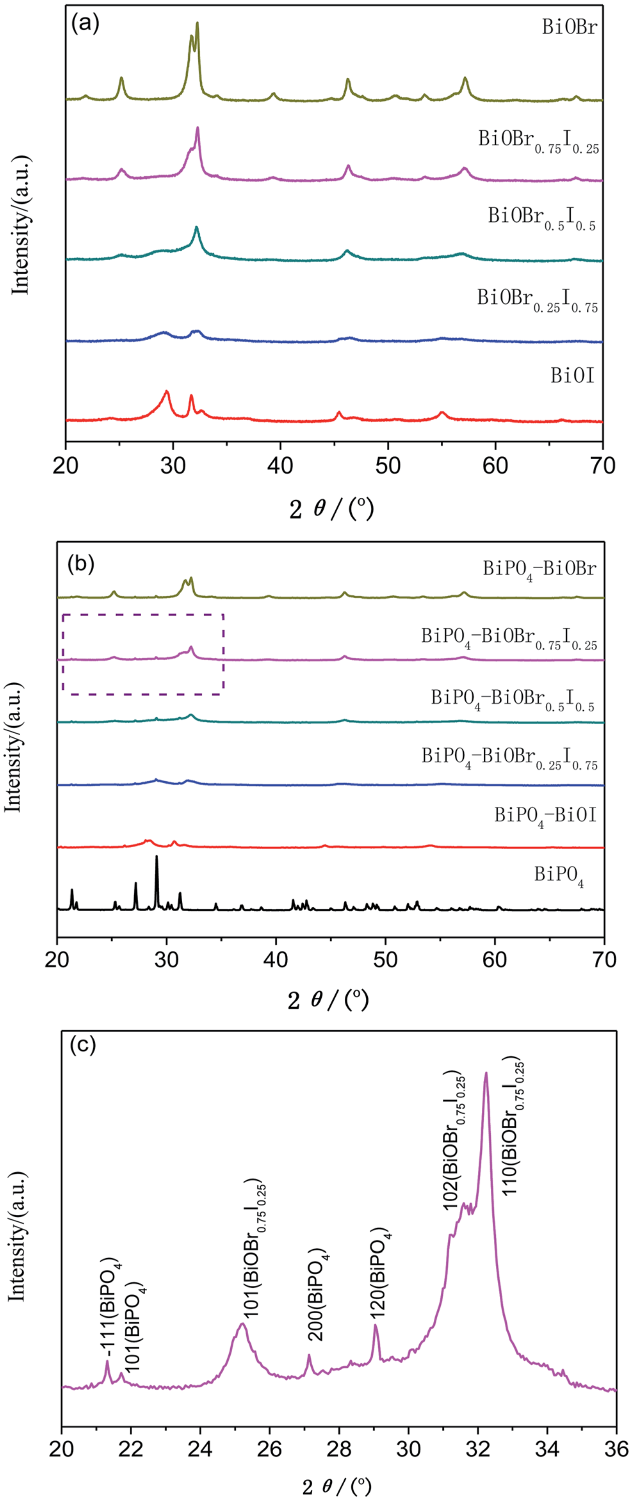

Fig. 2 XRD patterns of (a) $BiOBr_xI_{1-x}$ ($x = 0$, 0.25, 0.5, 0.75, 1) solid solutions; (b) 5% BiPO4–$BiOCl_xBr_{1-x}$ composites (c) the expanded XRD patterns of BiPO4–$BiOBr_{0.75}I_{0.25}$ in the range of $2\theta = 20$–36°.

shown in Fig. 1. It can be investigated that pure $BiPO_4$ (Fig. 1(a)) exhibited massive microcrystal with smooth surfaces, while $BiOBr_{0.75}I_{0.25}$ (Fig. 1(b)) was composed of microspheres with average diameter of about 1 μm. Fig. 1(c) displayed the SEM images of 5% $BiPO_4$–$BiOBr_{0.75}I_{0.25}$ composite. It can be discovered that the $BiPO_4$ microcrystal adhered well to the $BiOBr_{0.75}I_{0.25}$ microspheres, and no obvious morphology changes can be observed. The chemical element mapping analysis is carried out to further identify the composition of the composites. Fig. 1(d) presented the elemental mapping images of O, P, Br, I and Bi, respectively. It was considered that the brighter area in the elemental map always indicated a higher concentration of the corresponding element. It can be observed that the brighter area of P and Br showed the similar shape of the corresponding morphology of $BiPO_4$ and $BiOBr_{0.75}I_{0.25}$. Therefore, the elemental mappings may demonstrate the successful formation of the $BiPO_4$–$BiOBr_xI_{1-x}$ heterostructures through this facile solvothermal method.

The X-ray diffraction patterns of the as-synthesized $BiOBr_xI_{1-x}$ ($x = 0$, 0.25, 0.5, 0.75 and 1) and $BiPO_4$–$BiOBr_xI_{1-x}$ heterostructures were shown in Fig. 2. The distinct diffraction peaks in Fig. 2(a) suggested that all the samples were well crystallized. The diffraction patterns of as-obtained $BiOBr_xI_{1-x}$ solid solutions for $x = 0$ and $x = 1$ can be indexed to pure BiOI (JCPDS no. 10-0445) and pure BiOBr (JCPDS no. 09-0393) according to the standard card, respectively. It was obviously found that the $BiOBr_xI_{1-x}$ diffraction peaks shifted to a higher 2θ position with the increase of x value, which demonstrated the formation of the $BiOBr_xI_{1-x}$ solid solutions rather than the simple mixture of BiOI and BiOBr.[38] Fig. 2(b) displayed the diffraction patterns of $BiPO_4$ and the as-obtained 5% $BiPO_4$–$BiOBr_xI_{1-x}$ heterojunctions. As can be seen that all the $BiPO_4$–$BiOBr_xI_{1-x}$

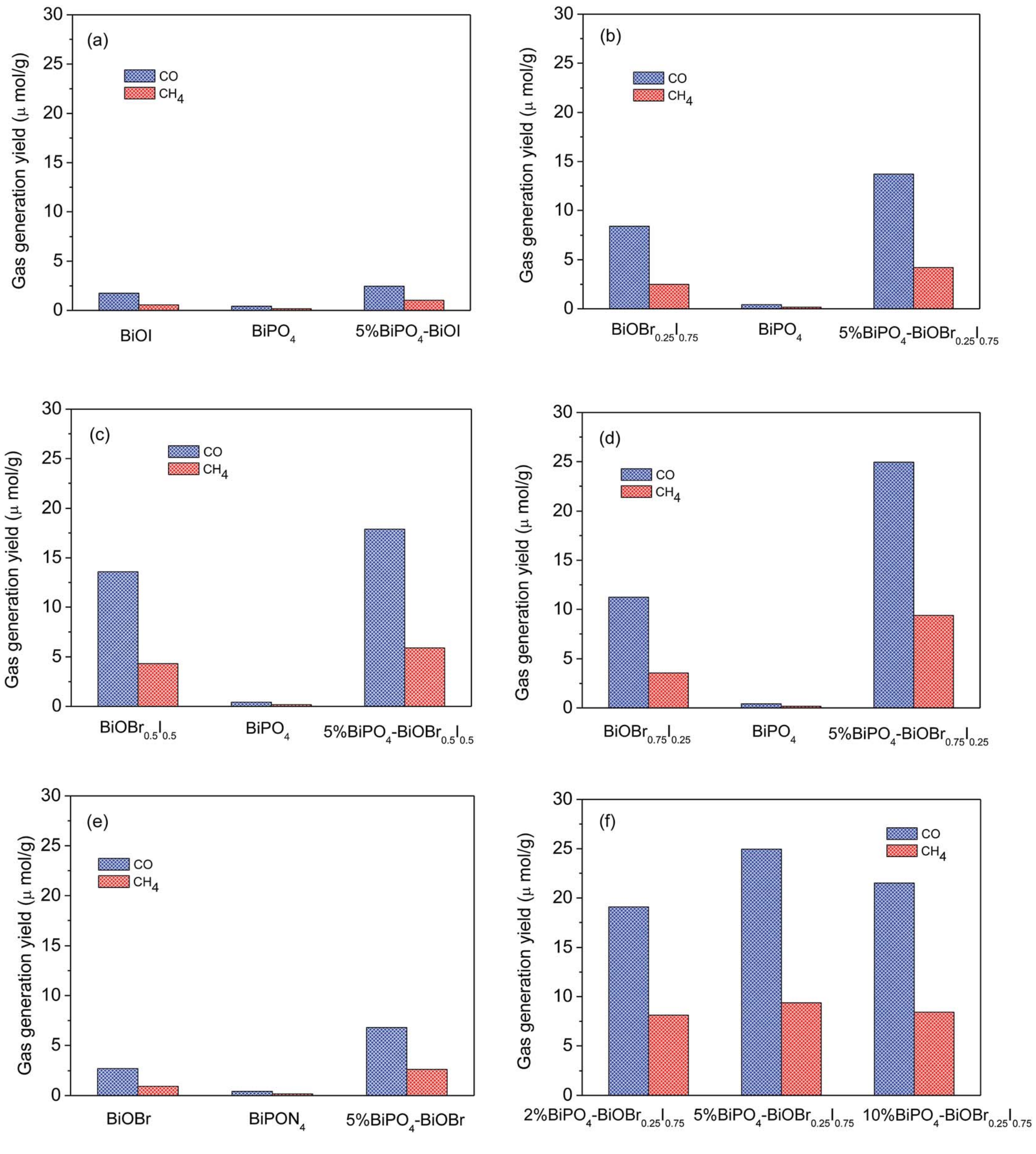

Fig. 3 CO and CH_4 yields on $BiOBr_xI_{1-x}$, 5% $BiPO_4$–$BiOBr_xI_{1-x}$ and $BiPO_4$ during 4 h light irradiation, respectively; (a) $x = 0$, (b) $x = 0.25$, (c) $= 0.5$, (d) $= 0.75$, (e) $= 1$ and (f) $BiPO_4$–$BiOBr_{0.75}I_{0.25}$ composites with different molar ratios at 3%, 5% and 10%. 5% under visible light irradiation.

heterojunctions have similar diffraction peaks with the typical $BiOBr_xI_{1-x}$ solid solutions. Fig. 2(c) showed the detailed expanded XRD patterns of the 5% $BiPO_4$–$BiOBr_{0.75}I_{0.25}$ heterojunctions with 2θ ranging from 20 to 36°. It can be distinctly investigated from the XRD of 5% $BiPO_4$–$BiOBr_{0.75}I_{0.25}$ heterojunctions that three diffraction peaks at $2\theta = 25.23°$, 31.59° and 32.25° were corresponded well to the (101), (102) and (110) crystal planes of the $BiOBr_{0.75}I_{0.25}$. While four weak peaks at $2\theta = 21.32°$, 21.72°, 27.13° and 29.04° can be indexed to the (−111), (101), (200) and (120) crystal planes of $BiPO_4$ (JCPDS no. 15-0767). Moreover, there were no other typical diffraction peaks of $BiPO_4$ being observed on these diffraction patterns, which may be due to the low amount of $BiPO_4$ and its well dispersion in these composites. Besides, no other impurities were detected in the XRD patterns of 5% $BiPO_4$–$BiOBr_xI_{1-x}$ heterojunctions.

Fig. 3 showed the photocatalytic CO_2 conversion activities of $BiPO_4$, $BiOBr_xI_{1-x}$ and $BiPO_4$–$BiOBr_xI_{1-x}$ heterojunctions under visible light irradiation ($\lambda > 420$ nm), which was evaluated by measuring the yield of main products of CH_4 and CO. As shown in Fig. 3(a–e), it can be easily found that all the heterojunctions displayed higher photocatalytic activity than the that of pure $BiPO_4$ and $BiOBr_xI_{1-x}$ solid solutions ($x = 0$, 0.25, 0.5, 0.75 and 1). Apparently, the 5% $BiPO_4$–$BiOBr_{0.75}I_{0.25}$ heterojunction photocatalyst showed the highest photocatalytic activity with the yield of CO and CH_4 up to 24.9 μmol g^{-1} and 9.4 μmol g^{-1}, respectively after 4 h of visible light irradiation. The optimal amount of $BiPO_4$ in $BiPO_4$–$BiOBr_{0.75}I_{0.25}$ photocatalyst was obtained by comparing the photocatalytic activities of different mole ratios of $BiPO_4$–$BiOBr_{0.75}I_{0.25}$ (2%, 5% and 10%) photocatalyst. As shown in Fig. 3(f), for the 2% $BiPO_4$–$BiOBr_{0.75}I_{0.25}$ and 10% $BiPO_4$–$BiOBr_{0.75}I_{0.25}$ samples, the yield of CO and CH_4 were about 19.1, 8.1 and 21.5, 8.4 μmol g^{-1} after 4 h of visible light irradiation, while the yield of CO and CH_4 over 5% $BiPO_4$–$BiOBr_{0.75}I_{0.25}$ were about 24.9 and 9.4 μmol g^{-1}. Therefore, the 5% $BiPO_4$–$BiOBr_{0.75}I_{0.25}$ heterojunction have the highest photocatalytic activity, and the optimum value of $BiPO_4$ content percentage should be 5%. Moreover, the results may also indicate that the optimal amount loading of $BiPO_4$ in the $BiPO_4$–$BiOBr_xI_{1-x}$ heterojunctions can have more effective contact, which may result in efficient transport of photogenerated electrons and holes.

The UV-vis diffuse reflectance spectroscopy (DRS) of the 5% $BiPO_4$–$BiOBr_xI_{1-x}$ heterostructures was displayed in Fig. 4(a). It can be found that the absorption edges of the 5% $BiPO_4$–$BiOBr_xI_{1-x}$ heterostructures were in the region of 430–650 nm, accompanying with the distinct red shift for the absorption edges with the increase of I. The DRS of the pure $BiPO_4$ and $BiOBr_xI_{1-x}$ solid solutions were shown in Fig. 4(b). The absorption edge of pure $BiPO_4$ photocatalyst was observed at about 295 nm, indicating that pure $BiPO_4$ was only in response to the UV light. Meanwhile, the $BiOBr_xI_{1-x}$ solid solutions showed a wide response within the visible light range, where the absorption edge extended to about 425–667 nm. It can be clearly seen that the absorption of all the $BiOBr_xI_{1-x}$ solid solutions exhibited significantly red shift with the increasing of I, which further proved the formation of the $BiOBr_xI_{1-x}$ solid solutions. Based on the DRS results, the band gap energy can be calculated according to the following equation:

$$A\left(h\nu - E_g\right)^{n/2} = \alpha h\nu \qquad (1)$$

where A was constant, h was Planck constant, ν was light frequency, E_g was the optical band gap energy, α was the absorption coefficient which was determined by scattering and reflectance spectra on the basis of Kubelka–Munk theory and n

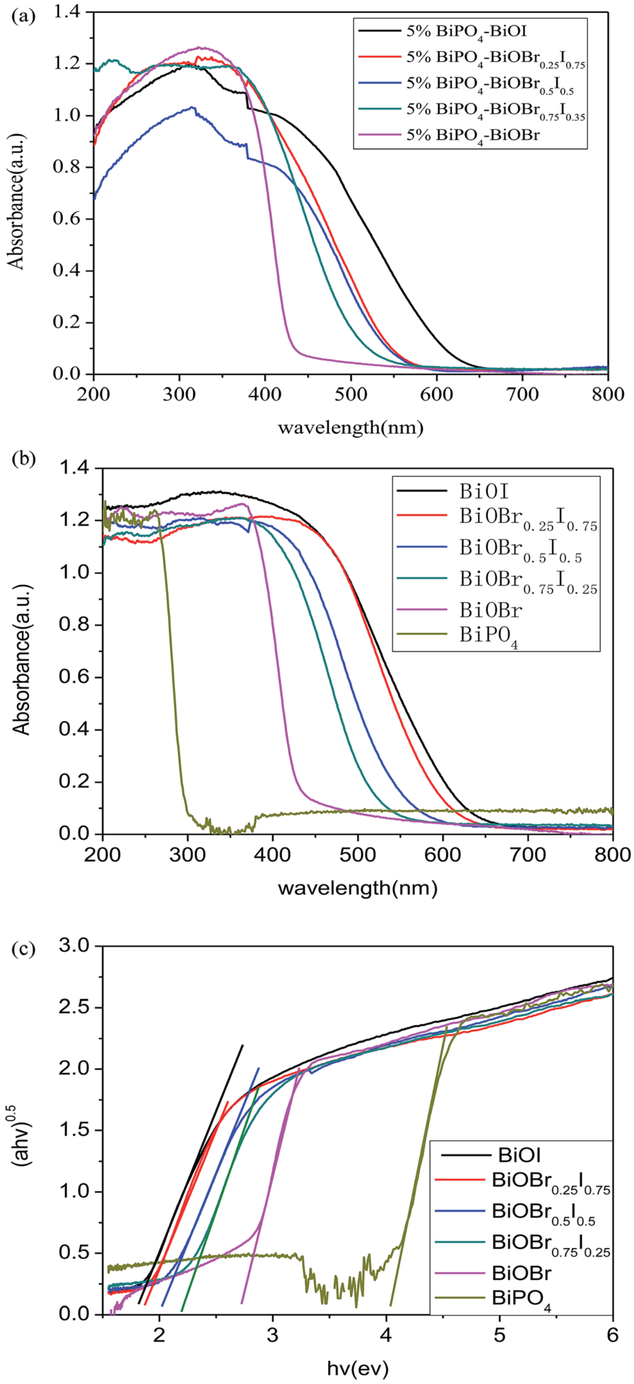

Fig. 4 UV–vis DRS spectrum of the as-fabricated (a) 5% $BiPO_4$–$BiOBr_xI_{1-x}$, (b) $BiOBrxI_{1-x}$ and $BiPO_4$ samples, respectively; (c) plots of the $(\alpha h\nu)^{1/2}$ *versus* $h\nu$ of $BiOBr_xI_{1-x}$ and $BiPO_4$ samples ($x = 0$, 0.25, 0.5, 0.75, 1).

was a coefficient related to the characteristic of the transition of the semiconductors ($n = 1$ for direct transition and $n = 4$ for indirect transition).[39] The plots of $(\alpha h\nu)^{n/2}$ *versus* $h\nu$ were shown in Fig. 4(c). The band gap (E_g) value of pure $BiPO_4$ was estimated to be 4.20 eV, while the E_g value of the $BiOBr_xI_{1-x}$ ($x = 0, 0.25, 0.50, 0.75$ and 1) solid solutions ranged from 1.86 to 2.92 eV with the increase of x. Moreover, the electric potentials of the valence band (VB) of $BiPO_4$ and $BiOBr_xI_{1-x}$ photocatalysts were also tested and the valence band XPS spectra and corresponding results of VB were shown in Fig. 5 and Table 1, respectively. Therefore, the CB positions of $BiPO_4$ and $BiOBr_xI_{1-x}$ can be calculated based on the energy gap and valence band XPS spectra of $BiPO_4$ and $BiOBr_xI_{1-x}$ photocatalysts. The E_{VB} and E_{CB} of $BiPO_4$ and $BiOBr_xI_{1-x}$ solid solutions were listed in Table 1. The results suggested that the E_{CB} and E_{VB} of $BiPO_4$ were estimated to be −0.96 eV and 3.24 eV. While the E_{CB} of $BiOBr_xI_{1-x}$ solid solutions ($x = 0, 0.25, 0.5, 0.75$ and 1) were 0.01, −0.06, −0.12, −0.21 and −0.64 eV, respectively. And the E_{VB} of $BiOBr_xI_{1-x}$ solid solutions were 1.87, 1.90, 2.04, 2.09 and 2.28 eV, respectively.

As the recombination rate of the photogenerated electrons and holes is an important factor influencing the activity of photocatalysts, the photocurrent was carried out to further identify the photocatalytic performance of $BiPO_4$–$BiOBr_xI_{1-x}$ heterojunctions. Fig. 6 displayed the photocurrent response of the pure $BiPO_4$, $BiOBr_xI_{1-x}$ solid solutions and 5% $BiPO_4$–$BiOBr_xI_{1-x}$ ($x = 0, 0.25, 0.5, 0.75$ and 1) heterojunctions measured with several light on/off cycles under the visible light irradiation. As can be observed, the photocurrent intensity of the 5% $BiPO_4$–$BiOBr_xI_{1-x}$ heterojunctions was higher than that of pure $BiPO_4$ and $BiOBr_xI_{1-x}$ solid solutions, confirming the obvious improvement of the separation efficiency of photoinduced electron–hole pairs and the effectively reduction of recombination rate. Therefore, the higher segregation efficiency and charge transfer may be the most important factors enhancing the photocatalytic activity of the 5% $BiPO_4$–$BiOBr_xI_{1-x}$ heterojunctions for the CO_2 conversion under visible light irradiation.

Based on the above results and analysis, the energy band structure diagram of the photocatalysts can be illustrated in Fig. 7. As can be seen that typical nested band structure can be obtained according to the energy band structures of individual $BiPO_4$ and $BiOBr_xI_{1-x}$, which is usually considered detrimental to the segregation of photogenerated carriers. However, the $BiPO_4$ was a typical n-type semiconductor photocatalyst, whose Fermi energy level was near the conduction band (CB). While $BiOBr_xI_{1-x}$ was a p-type semiconductor, with Fermi energy level

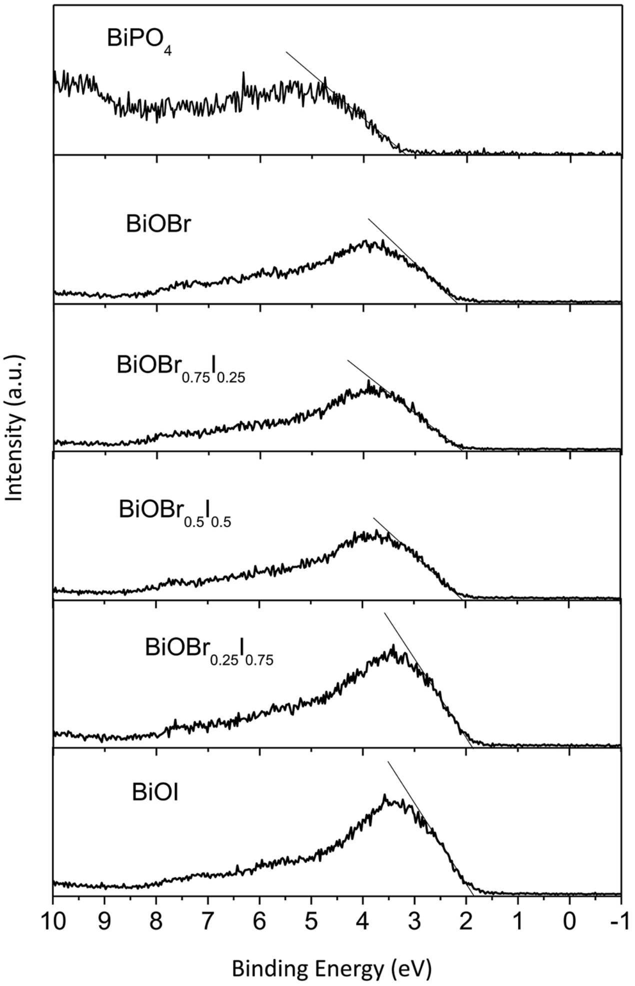

Fig. 5 Valence-band XPS spectra of $BiPO_4$ and $BiOBr_xI_{1-x}$ samples ($x = 0, 0.25, 0.5, 0.75, 1$).

Table 1 Absolute electronegativity, band gap energy, the VB edge and CB edge of as-synthesized $BiPO_4$ and $BiOBr_xI_{1-x}$ ($x = 0, 0.25, 0.5, 0.75, 1$)

	E_g (eV)	E_{VB} (eV)	E_{CB} (eV)
$BiPO_4$	4.20	3.24	−0.96
BiOI	1.86	1.87	0.01
$BiOBr_{0.25}I_{0.75}$	1.96	1.90	−0.06
$BiOBr_{0.5}I_{0.5}$	2.16	2.04	−0.12
$BiOBr_{0.75}I_{0.25}$	2.30	2.09	−0.21
BiOBr	2.92	2.28	−0.64

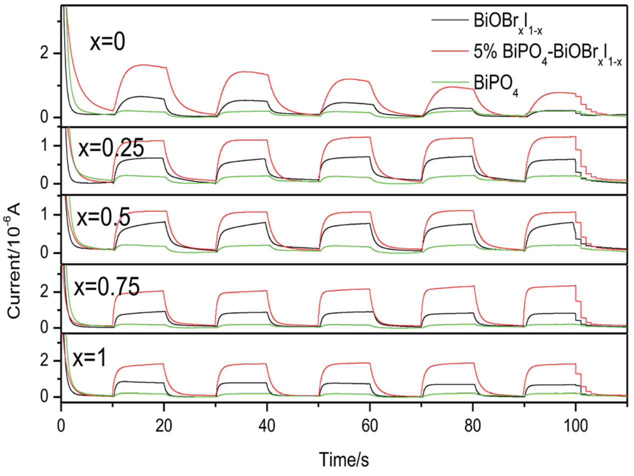

Fig. 6 Transient photocurrent response of pure $BiPO_4$, $BiOBr_xI_{1-x}$ and $BiPO_4$–$BiOBr_xI_{1-x}$ p–n junction ($x = 0, 0.25, 0.5, 0.75, 1$) under visible light irradiation.

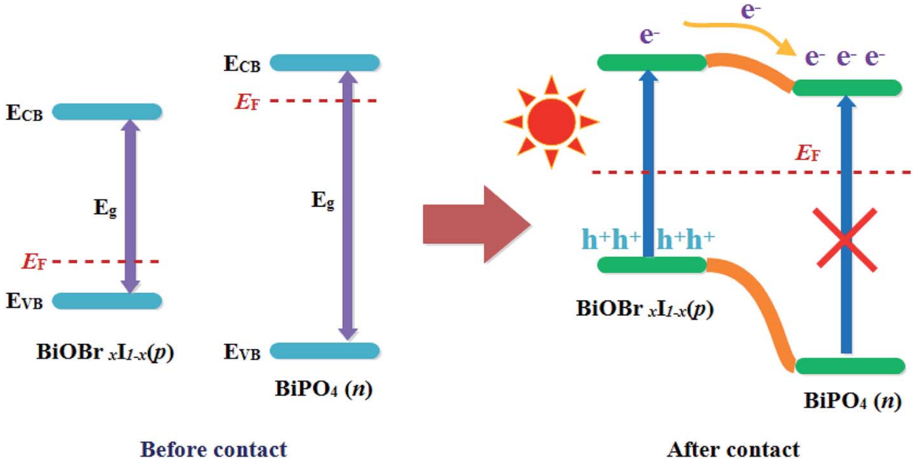

Fig. 7 Schematic diagram showing the energy band structure and electron–hole pair separation in the p–n heterojunction under visible light irradiation.

locating closely to the valence band (VB).[40,41] Therefore, according to the formation process of a typical p–n junction, when $BiPO_4$ contacted closely with the $BiOBr_xI_{1-x}$, the Fermi levels of p-type $BiOBr_xI_{1-x}$ and n-type $BiPO_4$ tend to move up and go down, respectively. Consequently, the whole energy band of $BiOBr_xI_{1-x}$ semiconductor will raise up whereas the energy band of $BiPO_4$ will descend to achieve an equilibrium state. Therefore, an inner electric field will be generated at the interface of the p–n junction, which was beneficial to the separation of photoinduced carriers.[42] At equilibrium, the region of $BiPO_4$ can be positively charged while the region of $BiOBr_xI_{1-x}$ may have negative charges due to the inner electric field between $BiPO_4$ and $BiOBr_xI_{1-x}$. Accordingly, the CB position of $BiPO_4$ became more positive than the CB position of $BiOBr_xI_{1-x}$. When the $BiPO_4$–$BiOBr_xI_{1-x}$ p–n heterojunctions was irradiated by visible light, the electron–hole pairs can be excited on $BiOBr_xI_{1-x}$. The photogenerated electrons on the CB bottom of p-$BiOBr_xI_{1-x}$ may transfer to the CB of n-$BiPO_4$, while the photogenerated holes still left on the VB of $BiOBr_xI_{1-x}$. Therefore, the photocatalytic performance can be greatly improved by the efficient separation of photoinduced electrons and holes in the established interactive band structures. Moreover, the difference of energy band in $BiOBr_xI_{1-x}$ ($x = 0$, 0.25, 0.5, 0.75 and 1) can not only affect the charge separation efficiency of $BiPO_4$–$BiOBr_xI_{1-x}$ ($x = 0$, 0.25, 0.5, 0.75 and 1) heterojunctions (which can investigated from Fig. 6), but also influence the light absorption property and position of energy band. As can be found from Table 1, the band gap of $BiOBr_xI_{1-x}$ became narrower with the increase of I in heterojunctions, which may enhance the visible light absorption and consequently result in the improved visible light photocatalytic activity. Although further increasing of I can lead to much narrower band gap, the CB level of $BiOBr_xI_{1-x}$ may shift more positively and VB level more negatively, indicating the lower oxidizability and reducibility on the VB and CB, which may be harmful to the photocatalytic ability. Therefore, rationally adjusting the energy band structures of $BiPO_4$–$BiOBr_xI_{1-x}$ heterojunctions can optimize the separation efficiency of photoinduced electron–hole pairs, light absorption property and interaction of energy band, thus resulting in the optimal visible light photocatalytic activity.

4. Conclusion

In summary, the $BiPO_4$–$BiOBr_xI_{1-x}$ p–n heterojunctions have been successfully prepared *via* a facile solvothermal method. All the heterojunctions showed the superior photocatalytic activity for the CO_2 conversion compared with pure $BiPO_4$ and $BiOBr_xI_{1-x}$ solid solutions under visible light irradiation. Among them, the 5% $BiPO_4$–$BiOBr_{0.75}I_{0.25}$ heterojunction displayed the highest photocatalytic efficiency. The enhanced photocatalytic activity was attributed to the effective separation of the photoinduced electron–hole pairs, increased visible light absorption property and interaction of the energy band. The construction of $BiPO_4$–$BiOBr_xI_{1-x}$ p–n heterojunction may provide a promising way to design high efficient photocatalysts with tunable band structure for environmental treatment and energy conversion.

Conflicts of interest

There are no conflicts to declare.

Acknowledgements

This work is financially supported by the National Nature Science Foundation of China (No. 21273034).

References

1 A. Fujishima and K. Honda, *Nature*, 1972, **238**, 37.
2 M. R. Hoffmann, S. T. Martin, W. Choi and D. W. Bahnemann, *Chem. Rev.*, 1995, **95**, 69.
3 R. Asahi, T. Morikawa, T. Ohwaki, K. Aoki and T. Taga, *Science*, 2001, **293**, 269.
4 H. G. Yang, C. H. Sun, S. Z. Qiao, J. Zou, G. Liu, S. C. Smith, H. M. Cheng and G. Q. Lu, *Nature*, 2008, **453**, 638.

5 X. L. Wang, H. L. He, Y. Chen, J. Q. Zhao and X. Y. Zhang, *Appl. Surf. Sci.*, 2012, **258**, 5863.
6 B. X. Lei, L. L. Zeng, P. Zhang, X. F. Zheng, Y. S. Wu, J. Fu and Z. F. Sun, *RSC Adv.*, 2014, **4**, 29099.
7 H. Y. Yin, X. L. Wang, L. Wang, Q. L. Nie, Y. Zhang and W. W. Wu, *Mater. Res. Bull.*, 2015, **72**, 176.
8 S. J. Li, J. L. Chen, Y. P. Liu, K. B. Xu and J. S. Liu, *J. Alloys Compd.*, 2019, **781**, 582.
9 J. Henle, P. Simon, A. Frenzel, S. Scholz and S. Kaskel, *Chem. Mater.*, 2007, **19**, 366.
10 X. X. Wang, Q. Ni, D. W. Zeng, G. L. Liao, Y. W. Wen, B. Shan and C. S. Xie, *Appl. Surf. Sci.*, 2016, **396**, 590.
11 L. F. Lu, L. Kong, Z. Jiang, H. H. C. Lai, T. C. Xiao and P. P. Edwards, *Catal. Lett.*, 2012, **142**, 771.
12 J. Cao, B. Y. Xu, H. L. Lin, B. D. Luo and S. F. Chen, *Chem. Eng. J.*, 2012, **185–186**, 91.
13 S. J. Li, S. W. Hu, W. Jiang, Y. Liu, Y. P. Liu, Y. T. Zhou, L. Y. Mo and J. S. Liu, *Front. Chem.*, 2018, **6**, 255.
14 S. J. Li, W. Jiang, K. B. Xu, S. W. Hu, Y. Liu, Y. T. Zhou and J. S. Liu, *Front. Chem.*, 2018, **6**, 518.
15 S. J. Li, S. W. Hu, W. Jiang, Y. Liu, J. S. Liu and Z. H. Wang, *J. Colloid Interface Sci.*, 2017, **501**, 156.
16 L. S. Zhang, H. L. Wang, Z. G. Chen, P. K. Wong and J. S. Liu, *Appl. Catal., B*, 2011, **106**, 1.
17 H. W. Huang, S. B. Wang, N. Tian and Y. H. Zhang, *RSC Adv.*, 2014, **4**, 5561.
18 S. J. Li, X. F. Shen, J. S. Liu and L. S. Zhang, *Environ. Sci.: Nano*, 2017, **4**, 1155.
19 S. J. Li, S. W. Hu, W. Jiang, Y. Liu, Y. T. Zhou, J. S. Liu and Z. H. Wang, *J. Colloid Interface Sci.*, 2018, **530**, 171.
20 Y. Guo, P. F. Wang, J. Qian, Y. H. Ao, C. Wang and J. Hou, *Appl. Catal., B*, 2018, **234**, 90.
21 C. S. Pan and Y. F. Zhu, *J. Mater. Chem.*, 2011, **21**, 4235.
22 Y. Guo, P. F. Wang, J. Qian, J. Hou, Y. H. Ao and C. Wang, *Catal. Sci. Technol.*, 2018, **8**, 486.
23 H. Xu, Y. G. Xu, H. M. Li, J. X. Xia, J. Xiong, S. Yin, C. J. Huang and H. L. Wan, *Dalton Trans.*, 2012, **41**, 3387.
24 C. S. Pan, J. Xu, Y. J. Wang, D. Li and Y. F. Zhu, *Adv. Funct. Mater.*, 2012, **22**, 1518.
25 K. Sayama, A. Nomura, Z. G. Zou, R. Abe, Y. Abe and H. Arakawa, *Chem. Commun.*, 2003, 2908.
26 C. S. Pan and Y. F. Zhu, *Environ. Sci. Technol.*, 2010, **44**, 5570.
27 J. Chen, J. X. Xia, J. Di, M. X. Ji, H. P. Li, H. Xu, Q. Zhang and J. Lu, *Colloids Surf., A*, 2016, **488**, 110.
28 H. F. Ye, H. L. Lin, J. Cao, S. F. Chen and Y. Chen, *J. Mol. Catal. A: Chem.*, 2015, **397**, 85.
29 F. F. Duo, Y. W. Wang, X. M. Mao, X. C. Zhang, Y. F. Wang and C. M. Fan, *Appl. Surf. Sci.*, 2015, **340**, 35.
30 C. R. Zheng, C. B. Cao and Z. Ali, *Phys. Chem. Chem. Phys.*, 2015, **17**, 13347.
31 J. Yuan, J. Wang, Y. She, J. Hu, P. Tao, F. Lv, Z. Lu and Y. Gu, *J. Power Sources*, 2014, **263**, 37.
32 Y. Feng, C. B. Liu, H. N. Che, J. B. Chen, K. Huang, C. Y. Huang and W. D. Shi, *CrystEngComm*, 2016, **18**, 1790.
33 W. J. Kim, D. Pradhan and B. K. Min, *Appl. Catal., B*, 2014, **147**, 711.
34 Y. L. Qi, Y. F. Zheng and X. C. Song, *J. Taiwan Inst. Chem. Eng.*, 2017, **71**, 355.
35 J. Yang, Y. J. Liang, K. Li, Y. l. Zhu, S. Q. Liu, R. Xu and W. Zhou, *J. Alloys Compd.*, 2017, **725**, 1144.
36 H. Gnayem and Y. Sasson, *ACS Catal.*, 2013, **3**, 186.
37 Z. F. Jia, F. M. Wang, F. Xin and B. Q. Zhang, *Ind. Eng. Chem. Res.*, 2011, **50**, 6688.
38 Q. Y. Liu, G. Han, Y. F. Zheng and X. C. Song, *Sep. Purif. Technol.*, 2018, **203**, 75.
39 Q. W. Cao, X. Cui, Y. F. Zheng and X. C. Song, *Alloys Intermet. Compd.*, 2016, **670**, 12.
40 Q. W. Cao, Y. F. Zheng, H. Y. Yin and X. C. Song, *J. Mater. Sci.*, 2016, **51**, 4559.
41 W. J. An, W. Q. Cui, Y. H. Liang, J. S. Hu and L. Liu, *Appl. Surf. Sci.*, 2015, **351**, 1131.
42 F. F. Duo, C. M. Fan, Y. W. Wang, Y. Q. Cao and X. C. Zhang, *Mater. Sci. Semicond. Process.*, 2015, **38**, 157.